IEEE Access
Multidisciplinary | Rapid Review | Open Access Journal

Received May 20, 2020, accepted May 25, 2020, date of publication May 28, 2020, date of current version June 10, 2020.

Digital Object Identifier 10.1109/ACCESS.2020.2998176

Magnetic Near-Field Strength Prediction of a Power Module by Measurement-Independent Modeling of Its Structure

JUNICHI KASHIWAGI, HIROYUKI SAKAIRI, HIROTAKA OTAKE, (Member, IEEE), YUSUKE NAKAKOHARA, AND KEN NAKAHARA, (Member, IEEE)
Research and Development Center, ROHM Co., Ltd., Kyoto 615-8585, Japan

Corresponding author: Junichi Kashiwagi (junichi.kashiwagi@dsn.rohm.co.jp)

ABSTRACT This paper presents a simulation scheme based on the S-parameters for simultaneously predicting the circuit operation of a power module (PM) and its consequent magnetic near-field (NF) strength. The PM comprises silicon carbide (SiC) metal-oxide-semiconductor field-effect transistors (MOSFETs). The circuit simulation is carried out using the S-parameterized PM aided by the SiC MOSFET die model, which allows for a precise replication of the switching waveforms. Note that the S-parameterized process needs no measurement data of the PM. The only experimental data are the characteristics of the specific SiC MOSFET dies used in the PM to adjust the die model. A buck converter is configured with the PM, and the magnetic NF radiated from the PM is measured in order to verify the validity of the proposed scheme. The magnetic field detection probe does not measure the magnetic field itself; instead, it measures the electromotive force (EMF) induced by the magnetic field. Accordingly, the simulated magnetic NF should be converted to the corresponding EMF, which enables a comparison of the measured and simulated results. This simulation scheme works successfully to predict the magnetic NF, but modeling the whole converter system is indispensable.

INDEX TERMS Power electronics, power module, S-parameter, circuit simulation, electromagnetic noise.

I. INTRODUCTION

Silicon carbide (SiC) and gallium nitride (GaN) transistors are devices that have been expected to exceed the performance limits demonstrated by their silicon (Si) counterparts in power electronics field. These so-called wide band-gap semiconductor power devices are characterized by their high-speed switching and high-frequency operation capability [1]–[3]. High-speed switching reduces the power loss in switching power supplies, while high-frequency operations miniaturize such power supplies [4]–[8].

However, high-speed switching and/or high-frequency operations multiply the time derivatives of voltage (dV/dt) and current (dI/dt) in switching power systems. Large dV/dt and dI/dt inevitably generate an unexpected current and voltage surge through the unavoidable distributed parasitic capacitances and inductances in circuit systems. This means that such power systems incessantly experience electromagnetic (EM) noise. EM noises deteriorate the operation quality of industrial equipment [9], but a time- and cost-consuming process is necessary to experimentally investigate the mechanism of EM noises and reduce them. Therefore, the EM noise prediction by the use of simulation technology is highly demanded, especially when large dV/dt and/or dI/dt are expected in the circuit.

The switching operation of transistors is the source of EM noise because it creates high-frequency components in the power application. Therefore, at first, simulation methods must be able to accurately reproduce the experimental switching waveforms in order to predict the EM noise. In addition, the expected simulation must be capable of predicting the near-field (NF) noise for estimating the far-field (FF) radiation noise because the international standard has restricted the acceptable radiation noise by using the electric field strength of FF radiation [10]. The NF noise determines the FF noise [11], [12].

Researchers are therefore focusing on the development of a simulation equipped with a-priori-assumption-independent

The associate editor coordinating the review of this manuscript and approving it for publication was Shihong Ding.

process to model the characteristics of parasitic passive components, such as capacitances and inductances, distributed anywhere in the circuit system. The equivalent circuit methodology is widely used to predict the current and voltage waveforms. In this methodology, the equivalent model of a target circuit must be expressed with the network of lumped-constant circuitry components [13]–[16]; however, no established standard can be used to determine a priori what the best equivalent circuit is. In particular, for a circuit that includes power modules (PMs), which often applies to industrial electronics—Engineers are always confronted with the difficulty of determining the locations of the parasitic components and the sizes of their constant, because the PMs include many semiconductor dies and a complicated interconnection structure. Furthermore, another kind of problem is evident in the equivalent circuit methodology for the FF noise simulation—the inability to calculate the radiation noise. In such a scheme where the lumped constants are used, it is impossible to model the space that surrounds the circuits.

In this paper, the authors propose a methodology to predict the circuit operation of a PM and its consequent magnetic NF strength simultaneously, and also describe the use of as few measurement results as possible during the modeling process. To predict the NF noise radiated from the converter, we adopt a buck converter comprising a PM equipped with two dies of SiC metal-oxide-semiconductor field-effect-transistors (MOSFETs) as the research object. In Section II, the authors verify the S-parameter calculation scheme for modeling the interconnection structure in a PM by using the frame structure thereof, i.e., no SiC dies in it (bare PM); the measured and simulated S-parameters are compared as functions of the input signal frequency. In Section III, a double pulse test (DPT) is carried out, using the PM in which two SiC MOSFET dies are used to construct the half-bridge. DPT is often carried out to evaluate the basic characteristics of a PM [17], [18]. In addition, the authors discuss the design of the S-parameter simulation configuration that corresponds to the DPT; verify whether or not the scheme works by comparing the simulated and experimental waveforms. In Section IV, the PM is used to configure the buck converter [19] with passive components, and the simulated counterpart is validated by measuring the magnetic NF strength being radiated from the PM. The magnetic NF strength is obtained from the EM/circuit co-simulation using the same S-parameter simulation configuration as in Section III. The used magnetic field detection probe does not detect the strength of the magnetic field itself, but it measures the electromotive force (EMF) induced by the radiated magnetic field that penetrates through the wire loop embedded in the probe. The discussion included in Section IV also addresses the transformation of the magnetic-field strength, which is the direct result of the EM/circuit co-simulation, to directly compare the measured results. Finally, we conclude this report in Section V.

II. CALCULATION SCHEME FOR THE S-PARAMETERS

The S-parameter scheme is a standard simulation configuration that is frequently used to analyze the behaviors of GHz-signal circuits in a printed circuit board (PCB) [20]. The S-parameters can also be applied to represent the input and output power interactions between circuit elements, such as packages, PMs, and PCBs used in power circuits. These interaction calculations represent the parasitic inductance, capacitance, and their mutual interactions. Hence, this scheme can simulate how the PM operates if the designated input signal is provided even without extracting the equivalent circuit.

In GHz-signal circuits, the reference plane is very important in the stabilization of the reference voltage; hence, PCBs are usually equipped with a wide metal plane working as a reference. In the S-parameter-based simulation, the ports representing the input and output of electric power are set between the reference plane and the points of analysis [20]. However, power electronic circuits have no such reference plane in their systems. Therefore, we first have to establish the setup of the simulation scheme to electromagnetically represent the PM used in this study.

For this purpose, the bare PM was prepared as shown in Fig. 1(a). This module had a three-layer structure comprising a copper plate on the surface and the bottom side, as well as an insulating substrate between the copper plates, which allowed for the transistors to structure a half-bridge circuit. As mentioned in Section I, the bare PM included no SiC dies in order to simplify the test circuit; instead, wire bonding was made to create a short circuit between all the tested terminals. Fig. 1(b) displays the experimental setup used to measure the S-parameters. The copper plate used as the reference plane was mounted such that it connects onto the Sub Miniature version A (SMA) connectors to straddle between them. The plate was positioned 5 mm away from

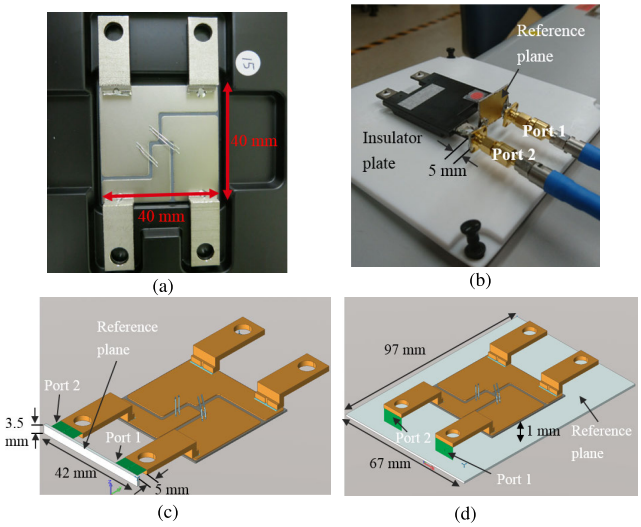

FIGURE 1. (a) Bare PM; (b) configuration for the S-parameter measurement; (c) Model A of the simulation; and (d) Model B of the simulation.

the inner edge of the terminals in the PM. A vector network analyzer (E5061B: Keysight Technologies, Inc.) was used to measure the S-parameters in the frequency range from 1 kHz to 3 GHz.

The first simulation model (Model A) used to replicate the setup situation shown in Fig. 1(b) is presented in Fig. 1(c), while the second simulation model (Model B) shown in Fig. 1(d) was equipped with the reference plane positioned 1 mm under the bottom plane of the PM. In the configuration used for Model B, all ports were set as referred to the wide reference plane as conventionally used in GHz-signal circuits [20], albeit differing from the experimental geometry. The S-parameters of both models A and B were calculated using an EM simulator (EMPro2017; Keysight Technologies, Inc.) that employed the finite element method.

Fig. 2 shows the experimental and simulated results of the S-parameters. Figs. 2 (a), (b), (c), and (d) exhibit $|S_{11}|$, $|S_{12}|$, $|S_{21}|$, and $|S_{22}|$ as functions of frequency, respectively. In each figure, the black, red, and blue lines denote the measured S-parameter spectrum and the simulated one of models A and B, respectively. Each figure includes an enlarged view of the 100 MHz-to-1 GHz spectra. $|S_{11}|$ and $|S_{22}|$ represent the reflectance of the input signal of each port, while $|S_{21}|$ and $|S_{12}|$ denote the transmittance of port-1 to 2 and port-2 to 1, respectively.

The simulation results based on Model A reproduced the experimental counterpart well, but the ones based on Model B failed to do so. This conclusion proves that the reference plane must be configured so as to replicate the experimental setup for extracting the S-parameters of an objective circuit system.

The abovementioned results in the simple two-port case must be applied to general multiple-port cases as well; thus, the position of the reference plane precisely replicates that of the measurement setup for a PM case. This remark for the reference plane preparation plays a crucial role in the precise prediction of how a PM operates.

III. REPLICATION OF SWITCHING WAVEFORMS

Fig. 3(a) shows the schematic of the DPT circuit used to verify the functionality of the proposed simulation scheme. The PM that used the same frame as the bare PM included the SiC MOSFET dies (S2301, ROHM Co., Ltd. [21]). The rectangle marked with a red dashed line denotes the part of the PM comprising the half-bridge in the DPT, while Q_1 and Q_2 represent the transistors. Fig. 3(b) shows the inner structure of the PM. The operating conditions of the circuit are as follows: the drain–source voltage (V_{ds}) = 600 V; the drain current (I_d) = 20 A; the external gate resistance (R_g) = 10 Ω; the input capacitor (C_{in}) = 3.5 mF; and the load inductance (L) = 500 μH. The low-side transistor, Q_2, was driven with the gate–source voltage (V_{gs}) = −5 V and 18 V to turn the transistor off and on, respectively. The high-side transistor, Q_1 maintained V_{gs} = −5 V throughout the test, as shown in Fig. 3(a).

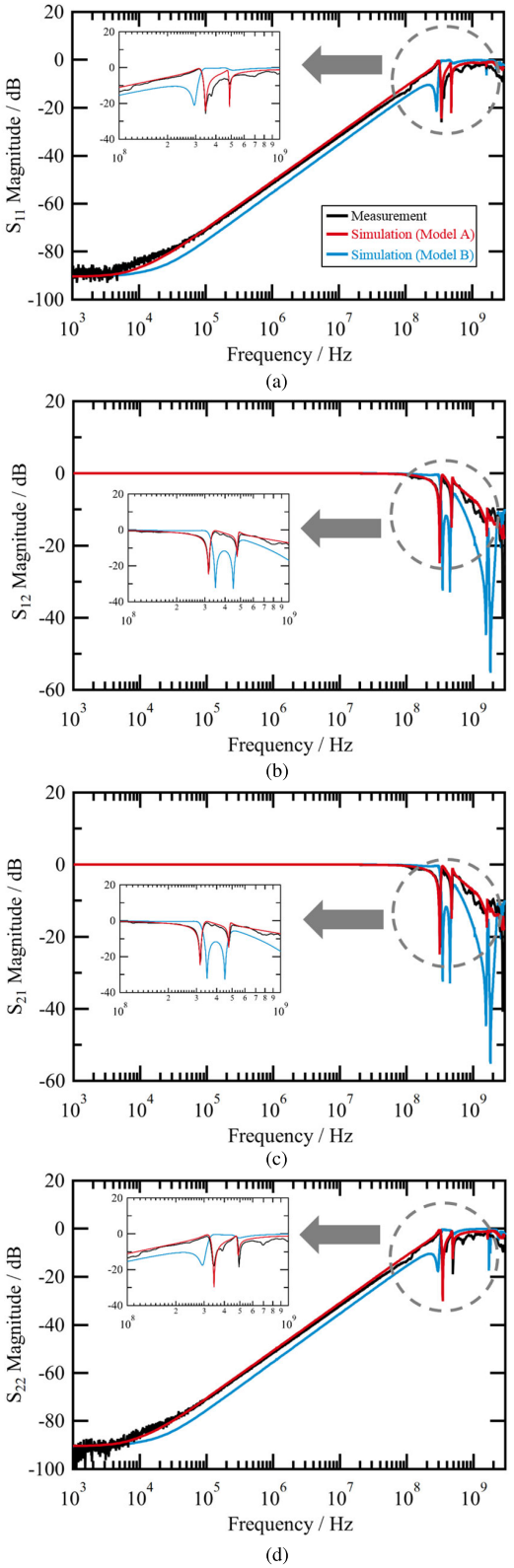

FIGURE 2. S-parameters of the bare PM. (a) $|S_{11}|$; (b) $|S_{12}|$; (c) $|S_{21}|$; and (d) $|S_{22}|$. The black, red, and blue lines denote the spectra of the S-parameters obtained by measurement, simulation based on Model A, and simulation based on Model B, respectively.

The circuit simulation process is presented herein. First, the SiC MOSFET die model was prepared. We have already

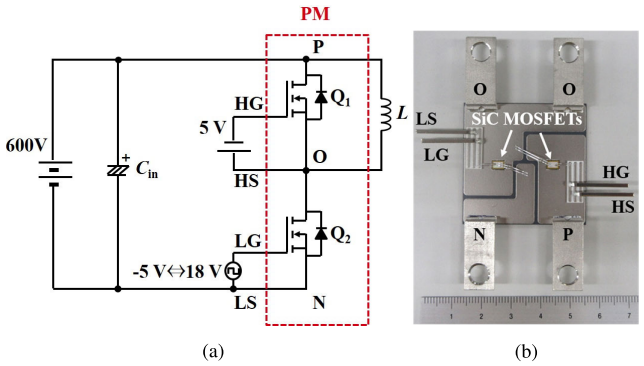

FIGURE 3. (a) Schematic of the DPT, where the symbols P, N, and O denote the terminals in the power line, whereas LS, LG, HS, and HG denote the gate-signal terminal; and (b) inner structure of the PM, where the capital-letter indices represent the circuit parts labeled as in Fig. 3(a).

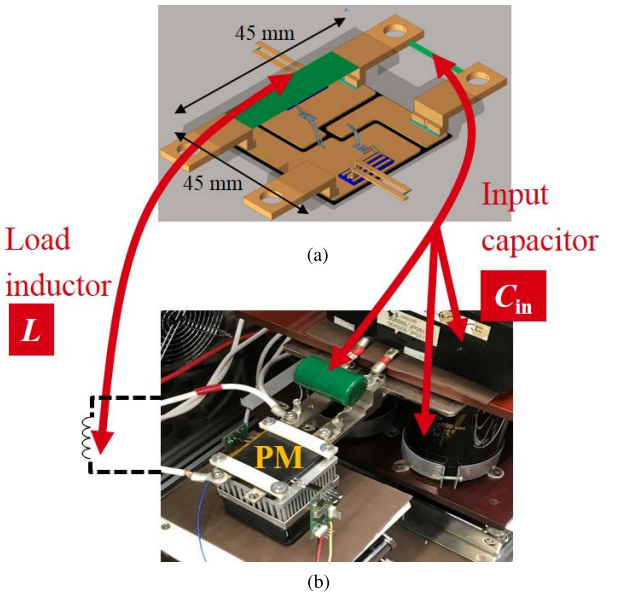

FIGURE 4. (a) S-parameter simulation model and (b) DPT setup.

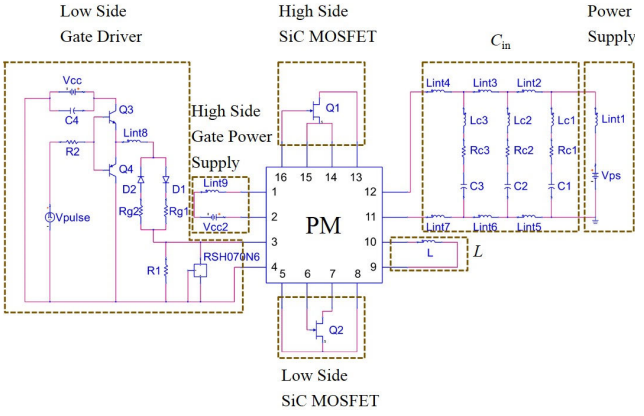

FIGURE 5. S-parameter circuit simulation schematic.

reported the die model of an SiC MOSFET to accurately reproduce its switching waveforms, and this model worked in the S-parameter scheme [22]. However, whether the circuit simulation using this die model is good or not depends on the measured data to characterize the device used for modeling. Thus, we modified the parameters of the model to reproduce the SiC MOSFET dies used in this study, in accordance with the fitting process reported in [22].

Secondly, the simulation model of the PM was created. The S-parameters of the bare PM were derived by EMPro, using the same port setting procedure described in Section II. During the process, the authors did not use any experimental data. The only things we used were the configuration design of the PM and the property data of its materials. Next, we imported the PM as an S-parameter component into the circuit simulator (ADS2017; Keysight Technologies, Inc.), and connected the S-parameterized bare PM to the SiC die model to create the PM model.

Fig. 4(a) shows the simulation configuration, while Fig. 4(b) displays the corresponding experimental setup. As noted in Section II, the ports were set between the terminals of the circuit components because the S-parameters represented the relationship between the input and output power. The S-parameter circuit simulation schematic is shown in Fig. 5, where the S-parameterized bare PM is represented with a blue rectangular box.

Figs. 6(a) and (b) show the turn-on and turn-off waveforms of the low-side device, respectively. The dotted lines indicate the experimental results, while the solid lines indicate the simulated results. The green, red, and blue lines represent the waveforms of V_{gs}, V_{ds}, and I_d, respectively. As the images show, the circuit simulation results using the S-parameterized PM successfully reproduced the experimental waveforms. Note that this simulation process required no priori assumptions or experimental data, except for the measured characteristics of the used devices. In the equivalent circuit methodology [13]–[16], priori assumptions or experimental data are always indispensable, because no universal algorithm exists to uniquely determine the equivalent circuit representing parasitic inductance or parasitic capacitance. On the other hand, the S-parameter scheme does not need the lumped-constant circuitry expression of components. The scheme spontaneously includes how parasitic components work and their interactions because it calculates the EM energy input–output relationship between the circuitry components. Therefore, this simulation scheme is appropriate for a front-loading design.

IV. MAGNETIC NF SIMULATION AND ITS VALIDATION

The authors also simulated the magnetic NF radiated from the PM with a buck converter as shown in Fig. 7(a). This simulation was carried out using ADS with EM/circuit co-simulation mode (EM circuit excitation) [23]. The PM takes the circuit part indicated by the red dashed line in Fig. 7(a). The operating conditions are as follows: the input voltage (V_{in}) = 400 V; the output voltage (V_{out}) = 80 V; the power inductor (L_p) = 2.5 mH; C_{in} = 3.5 mF; the output capacitance (C_{out}) = 100 μF; the load

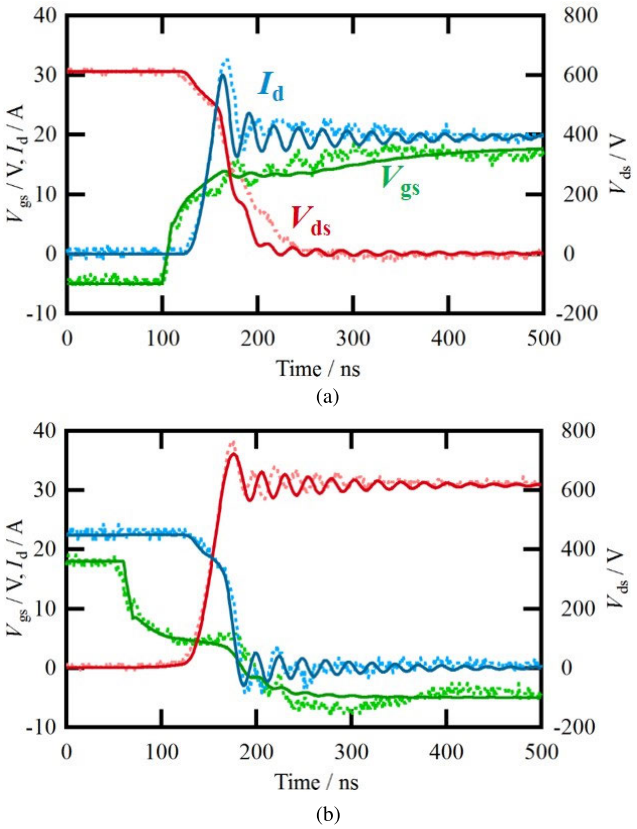

FIGURE 6. Waveforms of the low-side device: the experimental waveforms are represented by the dotted lines, while the simulated waveforms are denoted by the solid lines. The blue, green, and red colors are used to represent I_d, V_{gs}, and V_{ds}, respectively. (a) Turn-on and (b) turn-off waveforms.

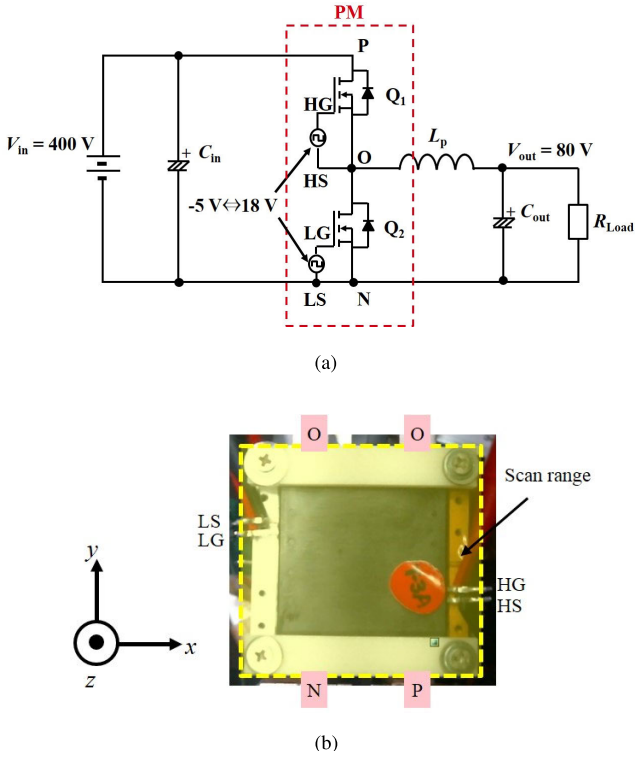

FIGURE 7. (a) Schematic of the buck converter circuit and (b) appearance of the PM in the buck converter, where the terminals are held by the metal beams. The yellow shaded area delineated by the yellow dashed line indicates the area over which the magnetic field probe scans. The capital-letter indices show the circuit parts as they are defined in Fig. 7(a).

resistance (R_{load}) = 13.3 Ω; and R_g = 0 Ω. V_{gs} was a rectangular pulse signal that alternates between −5 V and 18 V. A magnetic field probe (ESCO Technologies Inc.) with an embedded wire loop having a 5 mm radius was used to detect the EMF induced by the magnetic field that penetrates the loop. The axes of the Cartesian coordinate system (x, y, and z) are defined as shown in Fig. 7(b). The loop was set perpendicular to the x-, y-, and z- directions, at a height of 15 mm above the top surface (z = 0) of the PM. The probe scanned the yellow shaded area denoted in Fig. 7(b). In the following paragraphs, the symbols V_x, V_y, and V_z denote the x-, y-, and z-components of the measured EMF, respectively.

On the other hand, the ADS simulator calculatedly outputs the magnetic field, and not the EMF. This means that we cannot validate the accuracy of the simulation results by comparison with the experimental results. Thereby the authors have to establish the calculation process to derive the EMF from the simulated magnetic field results.

The total magnetic flux passing through a certain surface S perpendicular to the j direction ($j = x, y, z$), Φ_j, is expressed as follows:

$$\Phi_j = \mu_0 \int_S \mathrm{Re}\left\{H_j\left(\boldsymbol{r}, f, t\right)\right\} dS \tag{1}$$

where μ_0, $\boldsymbol{r}$, f, t, and H_j ($\boldsymbol{r}$, f, t) denote the permeability of vacuum, position vector, frequency, time, and the j direction component of the Fourier component associated with f of the steady-state complex magnetic field, respectively. Re $\{x\}$ denotes the real part of x. We want to obtain the EMF induced in the wire loop; thus, S is the area enclosed by the wire loop. H_j ($\boldsymbol{r}, f, t$) is defined as follows:

$$H_j\left(\boldsymbol{r}, f, t\right) = \left\{H_{j\mathrm{r}}\left(\boldsymbol{r}, f\right) + \mathrm{i}H_{j\mathrm{i}}\left(\boldsymbol{r}, f\right)\right\} \exp\left(-\mathrm{i}2\pi f t\right) \tag{2}$$

where $H_{j\mathrm{r}}$ ($\boldsymbol{r}, f$) and $H_{j\mathrm{i}}$ ($\boldsymbol{r}, f$) stand for the real and imaginary parts of the space Fourier part of H_j ($\boldsymbol{r}, f, t$), respectively, and i is the imaginary unit. From Faraday's law, the j direction component of the EMF induced by H_j ($\boldsymbol{r}, f, t$), V_j ($\boldsymbol{r}, f, t$), is expressed as:

$$V_j\left(\boldsymbol{r}, f, t\right) = \left| -\frac{d\Phi_j}{dt} \right| \tag{3}$$

Substituting (1) and (2) into (3), V_j ($\boldsymbol{r}, f, t$) becomes,

$$V_j\left(\boldsymbol{r}, f, t\right) = \mu_0 \left| -\frac{d}{dt} \int_S \mathrm{Re}\left[\left\{H_{j\mathrm{r}}\left(\boldsymbol{r}, f\right) + \mathrm{i}H_{j\mathrm{i}}\left(\boldsymbol{r}, f\right)\right\} \exp\left(-\mathrm{i}2\pi f t\right)\right] dS \right| \tag{4}$$

In (4), since S does not depend on t, we rewrite the ordinary derivative to the partial derivative and push it into the

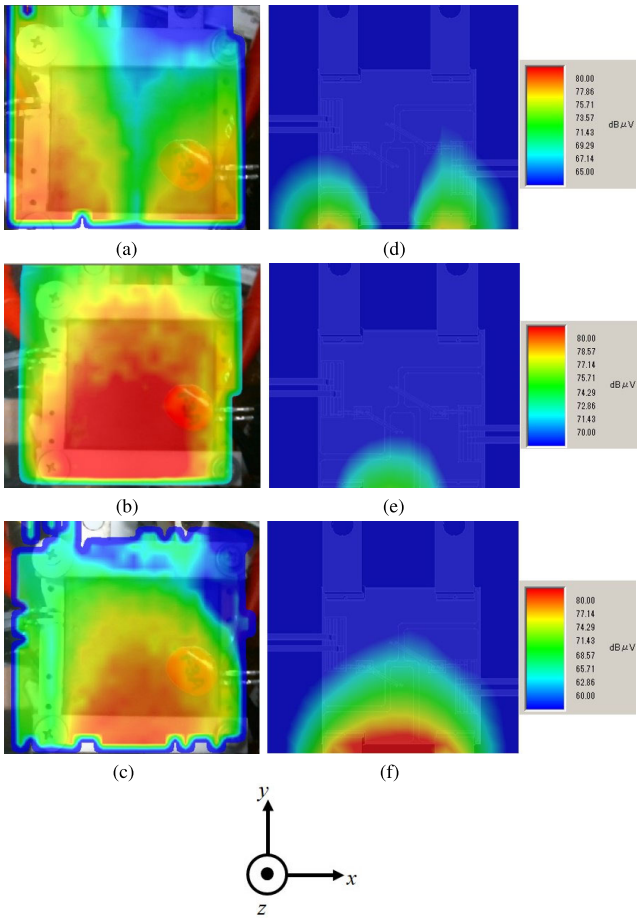

FIGURE 8. All figures are EMF mapping. (a), (b), and (c) are measured results, while (d), (e), and (f) are simulated results. (a) $V_x\ (r, f, t)_{max}$; (b) $V_y\ (r, f, t)_{max}$; (c) $V_z\ (r, f, t)_{max}$; (d) $V_x\ (r, f, t)_{max}$; (e) $V_y\ (r, f, t)_{max}$; and (f) $V_z\ (r, f, t)_{max}$.

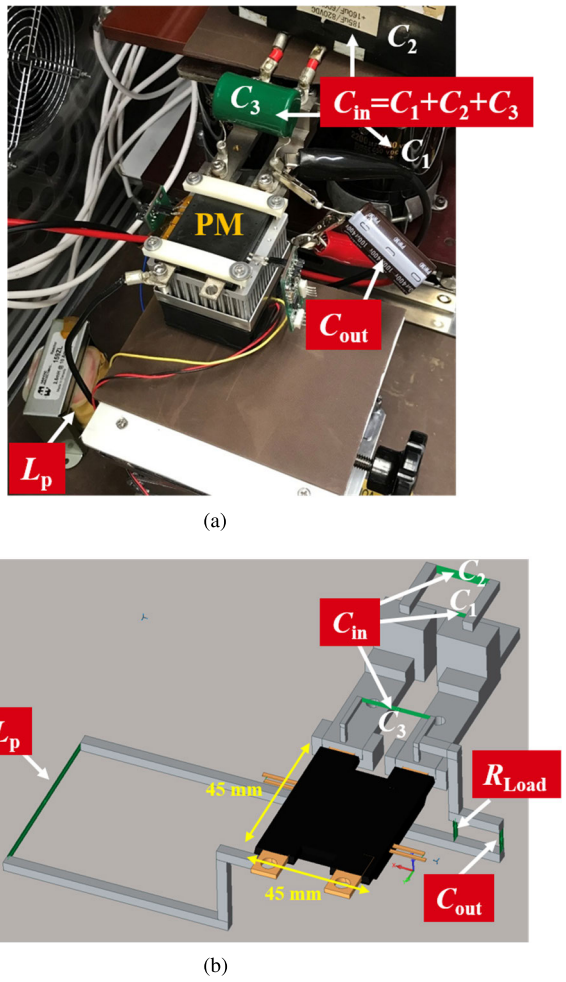

FIGURE 9. (a) Wide-range view of the buck converter configuration used to measure the magnetic NF and (b) modified simulation model.

integrand of the surface integral. Hence, $V_j\ (\boldsymbol{r}, f, t)$ becomes:

$$V_j\ (\boldsymbol{r}, f, t) = \mu_0 \Big| - \int_S \frac{\partial}{\partial t} \left\{ H_{jr}\ (\boldsymbol{r}, f) \cos\ (2\pi f t) + H_{ji}\ (\boldsymbol{r}, f) \sin\ (2\pi f t) \right\} dS \Big| \tag{5}$$

$$= 2\pi f \mu_0 \Big| \sin\ (2\pi f t) \int_S H_{jr}\ (\boldsymbol{r}, f)\ dS - \cos\ (2\pi f t) \int_S H_{ji}\ (\boldsymbol{r}, f)\ dS \Big| \tag{6}$$

$H_{jr}\ (\boldsymbol{r}, f)$ and $H_{ji}\ (\boldsymbol{r}, f)$ can be calculated using the outputs of ADS. So, the EM/circuit co-simulation provides $V_j\ (\boldsymbol{r}, f, t)$ from (6). The experimental V_x, V_y, and V_z were measured in the peak hold mode. The maximum value of $V_j\ (\boldsymbol{r}, f, t)$ at each position, denoted as $V_j\ (\boldsymbol{r}, f, t)_{max}$, was measured in the peak hold mode. $V_j\ (\boldsymbol{r}, f, t)_{max}$ was calculated for comparison with the experimental data.

The initial comparison between the simulated and the experimental results is summarized in Fig. 8. All the contour maps in Fig. 8 show the magnetic NF over the probe scanning area, where the color index denotes the EMF strength, $V_j\ (\boldsymbol{r}, f, t)_{max}$. The simulation was carried out using the configuration shown in Fig. 4(a), except for the port set between the P and O terminals being changed to be between the N and O terminals. This choice was made because the circuit used in this section was not a DPT circuit, but a buck converter. Figs. 8(a), (b), and (c) show the experimental results of $V_x\ (\boldsymbol{r}, f, t)_{max}$, $V_y\ (\boldsymbol{r}, f, t)_{max}$, and $V_z\ (\boldsymbol{r}, f, t)_{max}$, respectively, while (d), (e), and (f) show the calculated results of $V_x\ (\boldsymbol{r}, f, t)_{max}$, $V_y\ (\boldsymbol{r}, f, t)_{max}$, and $V_z\ (\boldsymbol{r}, f, t)_{max}$, respectively; $f = 60$ MHz was used for both. The same Cartesian coordinate system as in Fig. 7(b) was also used.

As Fig. 8 shows, the simulated results completely failed to reproduce the experimental results. The switching operation of the transistors was the source of the measured magnetic fields, and its waveforms were sufficiently reproduced, as seen in Fig. 6. This result implies a deficiency in the first simulation setup.

The measurement setup is shown in Fig. 9(a). It is inevitable that the high-f components generated by the transistor switching find the low-impedance paths, which usually include capacitance, to circulate in the circuit. Consequently, the high-f currents unintentionally flow through C_{in}, C_{out},

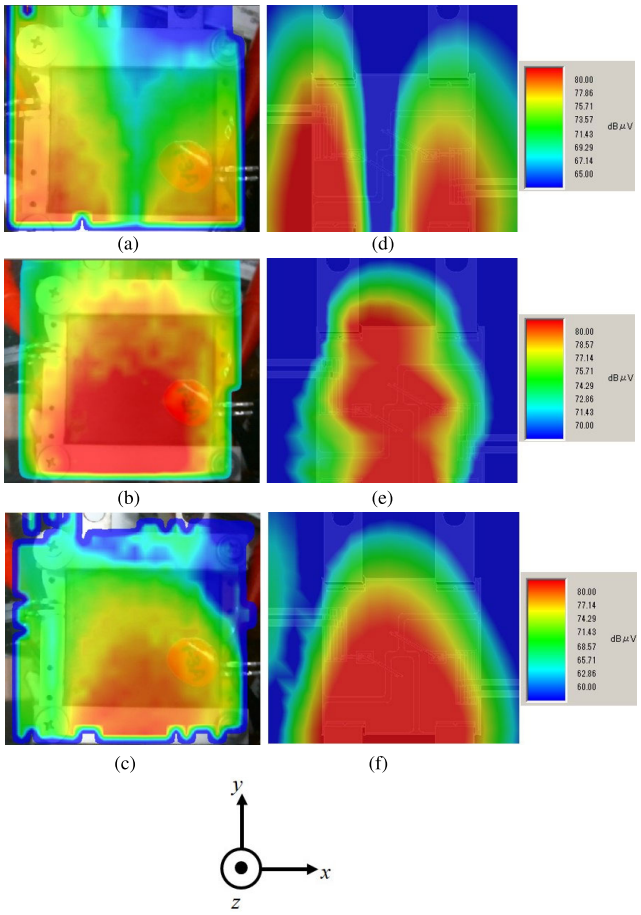

FIGURE 10. All figures are EMF mapping. (a), (b), and (c) are the same ones in Fig. 8 (a), (b), and (c) respectively, while the others represent the new simulated results; (d) $V_x\ (r, f, t)_{\max}$; (e) $V_y\ (r, f, t)_{\max}$; and (f) $V_z\ (r, f, t)_{\max}$.

and parasitic capacitor of L_p. This indicates that researchers have to consider this factor to predict the EM noise. Fig. 9(b) shows the modified model for the retry simulation. Its main difference from the first model was that the modified model included the wirings and bus bars. In addition, we set ports at the same position as the circuit components to duplicate the experimental circuit operation more precisely than that in the abovementioned case.

The second comparison between the simulated and experimental results is summarized in Fig. 10. All presented contour maps show a magnetic NF over the probe scanning area. Figs. 10(a), (b), and (c) show the same experimental maps as shown in Fig. 8, while Figs. 10(d), (e), and (f) depict the new simulated results based on the model in Fig. 9(b).

The new version of the simulated results successfully reproduced the experimental results in the spatial distribution and strength of the magnetic NF. This fact elucidates that the high-f current loops distributed in a system dominantly determined the magnetic NF. The NF is strongly related to the current causing conduction noise and propagates into the outer space to generate the FF. Hence, engineers must care for the whole configuration to design power systems.

The radiation noise and its consequent circuit malfunction [24] is a serious issue in designing power circuits. The methodology proposed herein to predict the NF without experimental data enables us to avoid the time-consuming processes of prototyping PM and also to effectively reduce noise sources beforehand.

V. CONCLUSION

We have proposed an S-parameter simulation methodology to predict the circuit operation of a PM and its consequent magnetic NF with no priori assumptions. Firstly, we showed that the S-parameters of the used bare PM can be compared well to the measured ones if the reference plate is positioned to correspond to the real situation. The S-parameterized PM was created by combining the S-parameterized bare PM with the die model of the SiC MOSFET, and it successfully generated the switching waveforms in the DPT. Next, we used a buck converter comprising the PM, and the magnetic NF radiated from the PM was simulated and measured. The magnetic field probe does not detect the magnetic field; instead, it detects the EMF induced by the magnetic field. Thus, the magnetic field as a simulation output was converted to the EMF before comparing the simulated and experimental magnetic NF. In addition, this study revealed that we must model the whole system to predict the magnetic NF, and that the proposed EM simulation also successfully predicted the measured magnetic field. In this proposed simulation scheme, no experiments by using the PM were mandatory. The only experimental data used were the characteristics of the SiC transistor.

This nearly experiment-independency provides many benefits in engineering design. This simulation enables virtually-performed multiple designing of the functions, the circuitry operations, and the radiating noise of PMs. These benefits will construct an excellent platform for the machine-learning-based technical design. In the near future, the research team will show a complete experiment-independent designing example of a PM by newly establishing the device simulation and electro-thermal co-simulation, and clarify the correlation between the performance of PMs and power systems including PMs.

REFERENCES

[1] T. Kimoto, "Material science and device physics in SiC technology for high-voltage power devices," *Jpn. J. Appl. Phys.*, vol. 54, no. 4, Apr. 2015, Art. no. 040103.

[2] J. Millán, P. Godignon, X. Perpiñà, A. Pérez-Tomás, and J. Rebollo, "A survey of wide bandgap power semiconductor devices," *IEEE Trans. Power Electron.*, vol. 29, no. 5, pp. 2155–2163, May 2014.

[3] B. J. Baliga, *Silicon Carbide Power Device*. Singapore: World Scientific, 2005, pp. 221–257.

[4] B. Whitaker, A. Barkley, Z. Cole, B. Passmore, D. Martin, T. R. McNutt, A. B. Lostetter, J. S. Lee, and K. Shiozaki, "A high-density, high-efficiency, isolated on-board vehicle battery charger utilizing silicon carbide power devices," *IEEE Trans. Power Electron.*, vol. 29, no. 5, pp. 2606–2617, May 2014.

[5] Y. Nakakohara, H. Otake, T. M. Evans, T. Yoshida, M. Tsuruya, and K. Nakahara, "Three-phase LLC series resonant DC/DC converter using SiC MOSFETs to realize high-voltage and high-frequency operation," *IEEE Trans. Ind. Electron.*, vol. 63, no. 4, pp. 2103–2110, Apr. 2016.

[6] T. Miyazaki, H. Otake, Y. Nakakohara, M. Tsuruya, and K. Nakahara, "A fanless operating trans-linked interleaved 5 kW inverter using SiC MOSFETs to achieve 99% power conversion efficiency," *IEEE Trans. Ind. Electron.*, vol. 65, no. 12, pp. 9429–9437, Dec. 2018.
[7] J. Kashiwagi, A. Yamaguchi, Y. Moriyama, and K. Nakahara, "Hysteretic control embedded boost converter operating at 25-MHz switching," *IEEE Trans. Circuits Syst. II, Exp. Briefs*, vol. 66, no. 1, pp. 101–105, Jan. 2019.
[8] D. Reusch, S. Biswas, and Y. Zhang, "System optimization of a high power density non-isolated intermediate bus converter for 48 v server applications," *IEEE Trans. Ind. Appl.*, vol. 55, no. 2, pp. 1619–1627, Mar. 2019.
[9] L. Rossetto, P. Tenti, and A. Zuccato, "Electromagnetic compatibility issues in industrial equipment," *IEEE Ind. Appl. Mag.*, vol. 5, no. 6, pp. 34–46, Nov./Dec. 1999.
[10] *Electromagnetic Compatibility of Multimedia Equipment—Emission Requirements*, CISPR, Geneva, Switzerland, Mar. 2015.
[11] X. Gao, J. Fan, Y. Zhang, H. Kajbaf, and D. Pommerenke, "Far-field prediction using only magnetic near-field scanning for EMI test," *IEEE Trans. Electromagn. Compat.*, vol. 56, no. 6, pp. 1335–1343, Dec. 2014.
[12] C. H. Schmidt, M. M. Leibfritz, and T. F. Eibert, "Fully probe-corrected near-field far-field transformation employing plane wave expansion and diagonal translation operators," *IEEE Trans. Antennas Propag.*, vol. 56, no. 3, pp. 737–746, Mar. 2008.
[13] N. Bondarenko, L. Zhai, B. Xu, G. Li, T. Makharashvili, D. Loken, P. Berger, T. P. Van Doren, and D. G. Beetner, "A measurement-based model of the electromagnetic emissions from a power inverter," *IEEE Trans. Power Electron.*, vol. 30, no. 10, pp. 5522–5531, Oct. 2015.
[14] T. Liu, T. T. Y. Wong, and Z. J. Shen, "A new characterization technique for extracting parasitic inductances of SiC power MOSFETs in discrete and module packages based on two-port S-Parameters measurement," *IEEE Trans. Power Electron.*, vol. 33, no. 11, pp. 9819–9833, Nov. 2018.
[15] Z. Miao, C.-M. Wang, and K. D. T. Ngo, "Simulation and characterization of Cross-Turn-On inside a power module of paralleled SiC MOSFETs," *IEEE Trans. Compon., Packag., Manuf. Technol.*, vol. 7, no. 2, pp. 186–192, Feb. 2017.
[16] I. Kovacevic-Badstübner, D. Romano, and J. Ekman, "A more accurate electromagnetic modeling of WBG power modules," in *Proc. ISPSD*, Chicago, IL, USA, 2018, pp. 260–263.
[17] H. Li, W. Zhou, X. Wang, S. Munk-Nielsen, D. Li, Y. Wang, and X. Dai, "Influence of paralleling dies and paralleling half-bridges on transient current distribution in multichip power modules," *IEEE Trans. Power Electron.*, vol. 33, no. 8, pp. 6483–6487, Aug. 2018.
[18] B. N. Torsaeter, S. Tiwari, R. Lund, and O.-M. Midtgard, "Experimental evaluation of switching characteristics, switching losses and snubber design for a full SiC half-bridge power module," in *Proc. IEEE 7th Int. Symp. Power Electron. Distrib. Gener. Syst. (PEDG)*, Vancouver, BC, Canada, Jun. 2016, pp. 1–8.
[19] R. W. Erickson, *Fundamentals of Power Electronics*, 2nd ed. Boston, MA, USA: Springer, 2001, pp. 13–37.
[20] J. Zhang, J. L. Drewniak, D. J. Pommerenke, M. Y. Koledintseva, R. E. Dubroff, W. Cheng, Z. Yang, Q. B. Chen, and A. Orlandi, "Causal RLGC(f) models for transmission lines from measured S-parameters," *IEEE Trans. Electromagn. Compat.*, vol. 52, no. 1, pp. 189–198, Feb. 2010.
[21] *S2301 N-Channel SiC Power MOSFET Bare Die Datasheet*. Rohm. Kyoto, Japan. Accessed: Apr. 21, 2020. [Online]. Available: https://fscdn.rohm.com/en/products/databook/datasheet/discrete/sic/mosfet/s2301-e.pdf
[22] H. Sakairi, T. Yanagi, H. Otake, N. Kuroda, and H. Tanigawa, "Measurement methodology for accurate modeling of SiC MOSFET switching behavior over wide voltage and current ranges," *IEEE Trans. Power Electron.*, vol. 33, no. 9, pp. 7314–7325, Sep. 2018.
[23] *Electromagnetic*. Keysight Technol., Santa Rosa, CA, USA, 2020. Accessed: May 7, 2020. [Online]. Available: http://edadownload.software.keysight.com/eedl/ads/2017/pdf/Electromagnetic.pdf
[24] M. Ramdani, E. Sicard, A. Boyer, S. Ben Dhia, J. J. Whalen, T. H. Hubing, M. Coenen, and O. Wada, "The electromagnetic compatibility of integrated circuits—Past, present, and future," *IEEE Trans. Electromagn. Compat.*, vol. 51, no. 1, pp. 78–100, Feb. 2009.

JUNICHI KASHIWAGI was born in Osaka, Japan, in 1982. He received the B.E. and M.E. degrees in electrical engineering from Kyoto University, Kyoto, Japan, in 2006 and 2008, respectively. In 2008, he joined ROHM Co., Ltd., Kyoto. From 2008 to 2012, he was engaged in the development of GaN laser diodes. Since 2013, he has been engaged in the development of system application of power device. His current research interests include simulation for EMC design and structural optimization for power devices using artificial intelligence technologies.

HIROYUKI SAKAIRI was born in Tochigi, Japan, in 1982. He received the B.S. degree in applied physics from the Tokyo University of Science, Tokyo, Japan, in 2007, and the M.Eng. degree in material science from the Nara Institute of Science and Technology, Nara, Japan, in 2009. He joined ROHM Co., Ltd., Kyoto, Japan, in 2009. From 2009 to 2012, he was engaged in the development of SiC power devices. Since 2013, he has been engaged in the development of system application of power device and modeling power device.

HIROTAKA OTAKE (Member, IEEE) was born in Chiba, Japan, in 1981. He received the B.Eng. and M.Eng. degrees in applied physics from Waseda University, Tokyo, Japan, in 2004 and 2006, respectively. He joined ROHM Co., Ltd., Kyoto, Japan, in 2006. From 2006 to 2011, he was engaged in feasibility study of GaN devices. From 2011 to 2017, he was engaged in the development of power modules and circuits using SiC devices. Since 2018, his current work is the development of GaN power devices.

YUSUKE NAKAKOHARA was born in Fukuoka, Japan, in 1987. He received the B.S. and M.S. degrees from Kyushu University, Fukuoka, in 2010 and 2012, respectively. He joined ROHM Co., Ltd., Kyoto, Japan, in 2012. From 2012 to 2018, he was engaged in the development of power conversion circuits. His current research interest includes development of optical output circuits.

KEN NAKAHARA (Member, IEEE) was born in Hyogo, Japan, in 1972. He received the B.S. degree in physics from Kyoto University, Kyoto, Japan, in 1995, and the Ph.D. degree in chemical from Tohoku University, Sendai, Japan, in 2010. He is currently the Head of the Research and Development Center, ROHM Co., Ltd., Kyoto. His current research interests are widely ranged from power electronics, material science, and energy devices to artificial intelligence technologies.